scientific reports

Check for updates

OPEN

A high-density multi-electrode platform examining the effects of radiation on in vitro cortical networks

Megan Boucher-Routhier[1], Janos Szanto[2], Vimoj Nair[2] & Jean-Philippe Thivierge[1,3]✉

Radiation therapy and stereotactic radiosurgery are common treatments for brain malignancies. However, the impact of radiation on underlying neuronal circuits is poorly understood. In the prefrontal cortex (PFC), neurons communicate via action potentials that control cognitive processes, thus it is important to understand the impact of radiation on these circuits. Here we present a novel protocol to investigate the effect of radiation on the activity and survival of PFC networks in vitro. Escalating doses of radiation were applied to PFC slices using a robotic radiosurgery platform at a standard dose rate of 10 Gy/min. High-density multielectrode array recordings of radiated slices were collected to capture extracellular activity across 4,096 channels. Radiated slices showed an increase in firing rate, functional connectivity, and complexity. Graph-theoretic measures of functional connectivity were altered following radiation. These results were compared to pharmacologically induced epileptic slices where neural complexity was markedly elevated, and functional connections were strong but remained spatially focused. Finally, propidium iodide staining revealed a dose-dependent effect of radiation on apoptosis. These findings provide a novel assay to investigate the impacts of clinically relevant doses of radiation on brain circuits and highlight the acute effects of escalating radiation doses on PFC neurons.

Keywords Radiation, Multielectrode array, Prefrontal cortex, Complexity, Functional connectivity, Neuronal activity

Radiation therapy and stereotactic radiosurgery are increasingly used to treat conditions such as primary and metastatic brain tumors, trigeminal neuralgia and intractable epilepsy[1,2]. Despite their widespread use, the effects of radiation on surviving neuronal networks remain poorly understood[2]. Radiation can produce brain injuries that occur on different timescales following treatment. Acute radiation-induced injuries typically occur within days of radiation, whereas early delayed injuries occur within one to six months post-radiation, and late delayed injuries occur over 6 months post-radiation[3,4]. Radiation-induced brain injuries have been associated with several cognitive impairments such as memory, attention, and executive function deficits, as well as reduced processing speed, which can occasionally progress to dementia[3,4,5]. These injuries appear to be dose-dependent, whereby patients who receive higher doses tend to have worse long-term outcomes[5].

Radiation-induced brain injuries are thought to be caused by a combination of cell death and dysfunction in surviving brain cells. Previous literature examining acute and early delayed effects of radiation has established that irradiated neurons show significantly increased firing rates[2,6], changes in synaptic morphology[2,7], and inhibited synaptic function and plasticity including deficits in long-term potentiation[4,8]. Larger doses of radiation (>60 Gy) in the primary visual cortex of Göttingen minipigs have also shown significant decreases in firing rate 6-months post-radiation suggesting distinct effects in acute compared to late delayed radiation-induced brain injuries[6].

Past research has primarily focused on the impact of radiation on the hippocampus due to its association with memory impairments. However, more recent work has highlighted the importance of studying other brain regions such as the prefrontal cortex (PFC). The PFC is a key region of interest because it is responsible for several important functions including executive function, decision-making, and working memory[9]. Neurons located within the PFC communicate with one another and with adjacent sensory, motor, and subcortical regions

[1]School of Psychology, University of Ottawa, 156 Jean-Jacques Lussier, Ottawa, ON K1N 6N5, Canada. [2]Department of Medical Physics, Division of Radiation Oncology, University of Ottawa, Ottawa, Canada. [3]University of Ottawa Brain and Mind Research Institute, 451 Smyth Rd, Ottawa, Canada. ✉email: jthivier@uottawa.ca

through precisely-timed action potentials that are impacted by radiation therapy[4, 10]. Further, the PFC has close functional connections with the hippocampus through a direct monosynaptic pathway that originates in the cornu ammonis 1 (CA1)/subiculum fields of the hippocampus and projects to the prelimbic and medial orbital areas of the PFC[4, 11]. Thus, the PFC is a major contributor to inter-regional hippocampal communication and a region of central importance in understanding cognitive impairments following radiation[2, 12].

Large-scale, high-density multi-electrode arrays (hd-MEAs) are gaining widespread interest as a tool to monitor brain networks in vitro[13]. Because of their ability to record from broad networks at high spatial and temporal resolution, hd-MEAs offer a middle ground between single-cell recordings and very large-scale neural activity obtained with electrocorticograms or electroencephalograms. State-of-the-art hd-MEAs can monitor thousands of neurons simultaneously at sufficient temporal resolution to isolate individual action potentials, providing a rich insight into patterns of network activity during both healthy and altered cortical states[14].

In this work, a novel assay was developed where hd-MEAs were employed to monitor the neuronal activity of in vitro PFC slices following radiation, with a focus on acute radiation-induced dysfunction. To the best of our knowledge, this is the first time that any MEA technology has been used to study the impacts of therapeutic doses of radiation on in vitro PFC circuits. Various markers were designed to quantify changes in network dynamics and apoptosis, including population firing rates, functional connectivity, graph-theoretic measures, and neural complexity. Comparisons of these markers between radiation and pharmacologically induced epileptiform activity revealed a distinct signature of radiation-induced changes in network function. These results suggest that hd-MEAs constitute a novel and viable assay to investigate the impact of clinically relevant doses of radiation[15, 16] on neuronal dysfunction and apoptosis.

Results

Irradiated brain slices reveal changes in cortical population activity

Neuronal activity recorded on the hd-MEA was characterized by sharp deflections in voltage at individual channels, indicative of multi-unit spikes amongst clusters of neurons in the vicinity of the electrodes (Fig. 1A). These deflections were detected by application of a threshold below the mean of the voltage (see "Methods"). The rate of neural activity at individual channels was computed as the average number of a pronounced increase in firing rate was observed following PE treatment (mean rate of 2.25 Hz compared to a baseline firing rate of 0.09 Hz, $p = 4.9558e{-}39$). Further work characterizing epileptiform activity in terms of propagating waves can be found elsewhere[17]. These results show that radiation-induced changes in neuronal activity remained markedly lower than epileptiform activity.

Threshold-crossing events per second and stored as rasters for offline analysis. These rasters revealed an increase in activity among radiated slices compared to controls (Fig. 1B). A dose of 20 Gy radiation yielded a statistically reliable increase in mean firing rate compared to sham radiation (Wilcoxon rank sum test, $p = 2.4546e{-}27$), as did 50 Gy ($p = 7.2954e{-}05$) and 100 Gy ($p = 0.0028935$). Examples of individual rasters are shown in Fig. 1C, where individual dots identify the times and channels where these events occurred.

Probing alterations in functional connectivity

Next, we examined functional connectivity amongst cortical neurons by computing correlations between all pairs of channels on the hd-MEA (Fig. 2A, B). Functional connectivity is indicative of the communication amongst populations of neurons and is known to fluctuate in disease states[18, 19, 20, 21]. To facilitate the interpretation of functional networks, a cut-off of $r = 0.2$ was applied to reject lower correlations amongst pairs of channels.

Two markers of functional connectivity were examined, namely the strength and the number of functional connections across conditions. The strength of functional connectivity following radiation was higher than controls across all doses of radiation delivered to the PFC slices (Fig. 2C). Functional connections were significantly stronger than controls for 50 Gy ($p = 0.0014797$) but did not reach statistical significance for 20 Gy ($p = 0.08826$) or 100 Gy ($p = 0.16837$). Despite variability across conditions, the overall impact of radiation was an increase in the strength of functional connections across PFC networks, indicative of greater synchronization amongst neurons.

In radiated slices, the number of functional connections showed a dose-dependent response, with higher doses yielding more abundant connections than lower doses (Fig. 2D). The number of functional connections was higher than controls for 20 Gy ($p = 3.3951e{-}07$), 50 Gy ($p = 2.2621e{-}11$) and 100 Gy ($p = 1.9287e{-}19$). Thus, radiation impacted PFC functional connectivity by increasing the density of connections amongst pairs of channels on the array.

These results were compared to networks that received PE treatment (Fig. 2B). The mean strength of functional connectivity was markedly higher in PE compared to radiated slices (20 Gy: $p = 9.543e{-}14$; 50 Gy: $p = 1.4247e{-}13$; 100 Gy: $p = 3.3604e{-}11$), suggesting an increase in synchrony during PE activity. Conversely, the number of functional connections was lower in PE compared to radiated slices (20 Gy: $p = 1.3018e{-}40$; 50 Gy: $p = 2.6966e{-}39$; 100 Gy: $p = 3.578e{-}39$). The lower number of connections obtained under PE treatment is explained by epileptiform activity yielding functional interactions that are focused on a small group of neurons within the broader population recorded on the array (Fig. 2B). Indeed, seizure-like events observed under PE are characterized by a spatially-focused propagation of strong and repeatable patterns of activity[17]. In sum, radiation induced more abundant functional connections amongst PFC neurons. These results are distinct from epileptiform activity, where strong connections are present but are much sparser due to spatially focused epileptiform propagation across the array.

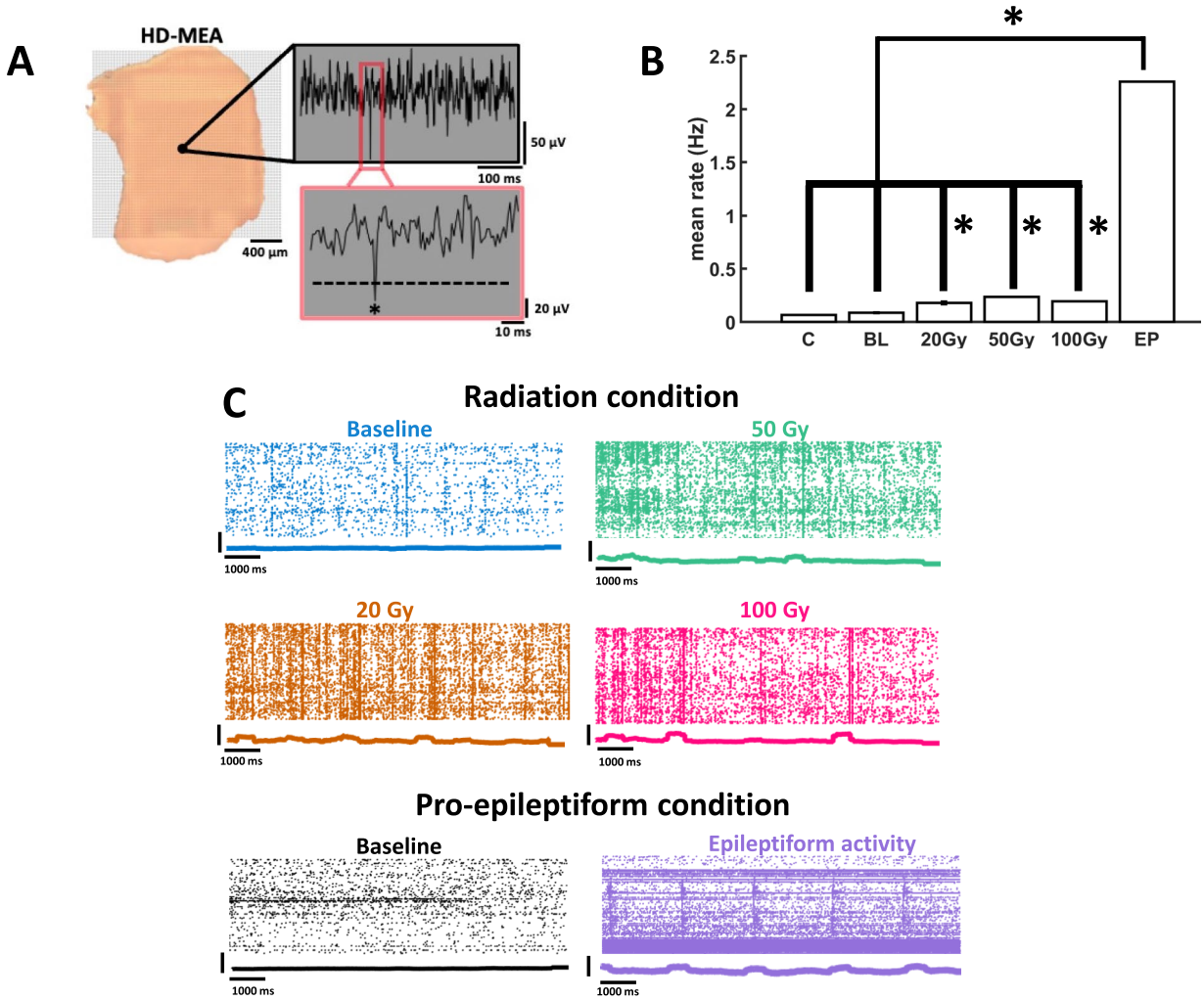

Fig. 1. Neuronal activity in populations of prefrontal cortical neurons. (**A**) *Left*, example of PFC slice placement on the hd-MEA. *Right*, multiunit spike (identified by an asterisk "*") extracted from voltage deflections identified at an individual channel. (**B**) Mean firing rate of prefrontal cortical neurons across various conditions. C = control slices for the radiation treatment; BL = baseline in the PE condition; 20–100 Gy = radiation conditions; EP = epileptiform activity. *indicates statistical significance at $p < 0.01$. (**C**) Rasters of activity show spikes across whole populations of neurons following graded doses of radiation or perfusion of pro-epileptiform solution. Peri-stimulus time histogram underneath each raster shows summated activity using a 500 ms rolling window.

Graph-theoretic measures of functional networks

Functional networks were further characterized by examining five graph-theoretic metrics, namely modularity, global efficiency, local efficiency, assortativity, and transitivity[22]. The *modularity* of a network reflects the extent to which nodes may be divided into non-overlapping modules, where nodes within a module share a high number of connections. Relative to baseline networks, epileptiform (EP) networks attained lower modularity ($p = 8.6735e{-}28$) (Fig. 3A). A lower dose of radiation (20 Gy) yielded a moderate increase in modularity relative to controls ($p = 2.2264e{-}08$), but no effect was found at higher doses (50 Gy and 100 Gy). Hence, epileptiform activity decreased the modularity of functional networks, but no reliable alteration was found across radiated networks.

The *global efficiency* of functional networks computes the average of inverse shortest paths between nodes. Networks where only a few connections need to be traversed between pairs of nodes have a high global efficiency. We found high global efficiency in functional networks following radiation (20 Gy: $p = 1.4813e{-}20$; 50 Gy: $p = 3.3595e{-}26$; 100 Gy: $p = 5.9097e{-}28$) (Fig. 3B). This effect was not replicated in EP networks, where global efficiency remained low. We reasoned that this result may be due to EP networks occupying a delimited region on the array (Fig. 2B). To control for this effect, we computed *local efficiency*, which measures the connections around individual connected nodes. Local efficiency yielded a significant increase in EP networks relative to baseline ($p = 1.4638e{-}30$), consistent with the idea that EP increases local efficiency around. Individual nodes participating in epileptiform activity (Fig. 3B). Local efficiency was also increased in radiated networks (20 Gy: $p = 1.4651e{-}08$; 50 Gy: $p = 4.1548e{-}12$; 100 Gy: $p = 4.8439e{-}14$).

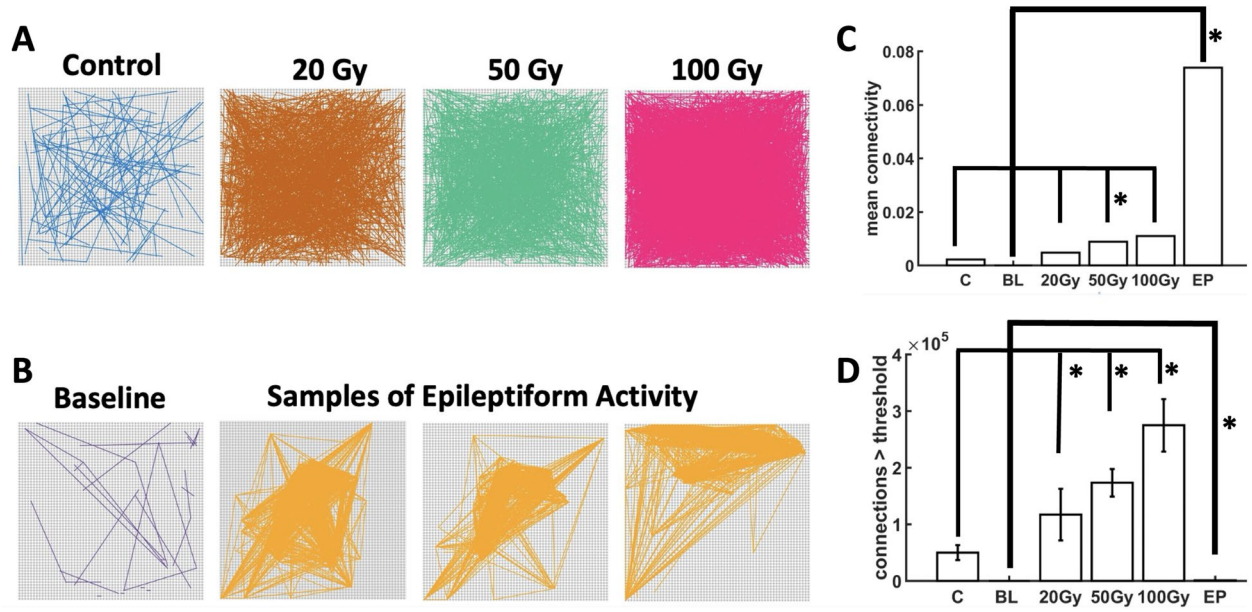

Fig. 2. Functional connectivity of cortical networks. Radiation (**A**). Perfusion of a pro-epileptiform (PE) solution (**B**). Mean strength (**C**) and number of functional connections exceeding a pre-defined threshold (**D**). Asterisks ("*") indicate significance at $p < 0.01$ (Wilcoxon rank sum test).

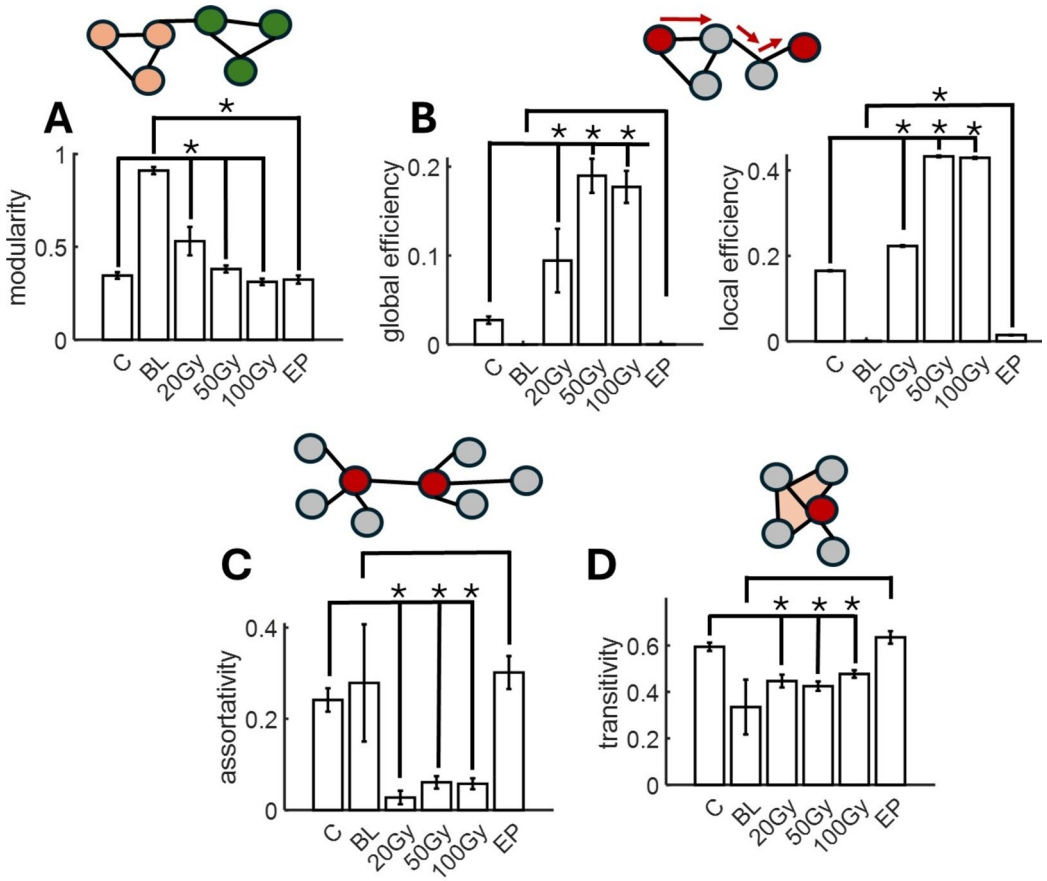

Fig. 3. Graph-theoretic properties of functional connectivity. Modularity (**A**), global and local efficiency (**B**), assortativity (**C**), and transitivity (**D**) were computed across experimental conditions. A cartoon illustration of each measure is shown above figures.

Network *assortativity* determines the extent to which pairs of nodes that are connected together have a similar number of connections (technically termed the degree of a node) to other nodes in the network. As an illustration, Fig. 3C shows two nodes that have the same number of connections, and hence high assortativity. We found a decrease in assortativity in radiated networks (20 Gy: $p = 6.0098e{-}16$; 50 Gy: $p = 3.5354e{-}12$; 100 Gy: $p = 6.4025e{-}14$), but no reliable change for EP networks.

The *transitivity* of a network measures the extent to which pairs of nodes that are connected together also share a common neighbor. Visually, functional networks with high transitivity show closed triangles between triples of nodes (Fig. 3D). We found a moderate decrease in transitivity for radiated slices relative to controls (20 Gy: $p = 5.7301e{-}07$; 50 Gy: $p = 1.6429e{-}08$; 100 Gy: $p = 1.0579e{-}07$). No such effect was reported for EP networks.

Taken together, graph-theoretic measures of functional networks revealed different classes of metrics, where some metrics are preferentially altered in radiated networks (global efficiency, assortativity, and transitivity), while others are altered more specifically in EP networks (modularity) or for both radiation and EP (local efficiency). These measures of functional connectivity open a potentially rich field of investigation into network-level alterations under a variety of neuronal states and conditions.

Global synchronization

To examine alterations in synchronization induced by radiation and PE, we began by temporally averaging spike rasters using a 500 ms rolling window, then computed the peri-stimulus time histogram (PSTH) by summing activity across channels. Next, we calculated the correlation between spikes at individual channels and the PSTH (Fig. 4A). A high correlation is indicative of global synchronization between each neuron and fluctuations in population activity. Overall, high radiation (100 Gy) significantly increased synchronization (Fig. 4B) ($p = 0.00022411$), but not lower doses (20 Gy: $p = 0.22818$; 50 Gy: $p = 0.11252$). Global synchronization increased only marginally in EP networks ($p = 0.018383$), for two probable reasons. First, periods of epileptiform activity are interspersed by intervals of quiescent activity with no marked synchrony[17]. Second, epileptiform activity remained spatially delimited (Fig. 2B), thus limiting global synchronization. Comparable results were obtained when lowering the rolling window to 250 ms (Fig. 4C). Thus, an increase in global synchronization was obtained with high radiation doses and did not emerge from lower radiation doses or epileptiform activity.

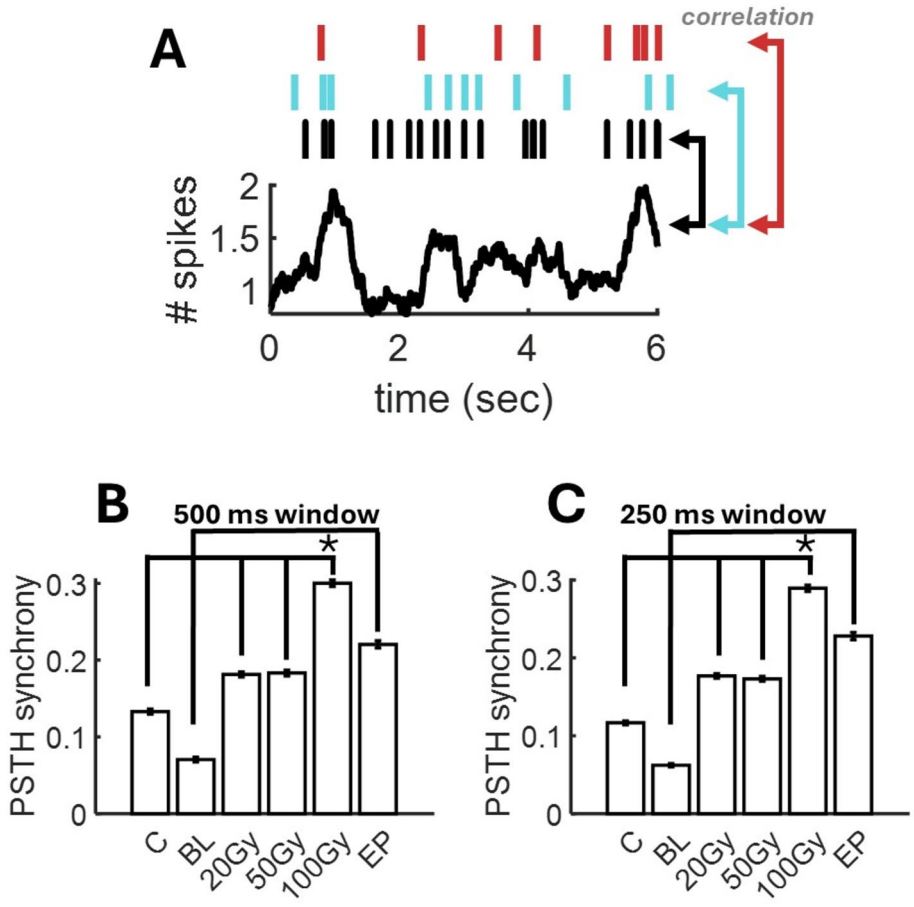

Fig. 4. Alterations in global synchronization. (**A**) Synchronization is computed by the correlation between spikes at individual channels (top) and the PSTH obtained by summing all neurons in the population after averaging with a rolling temporal window. (**B**-**C**) Mean synchronization across conditions using a rolling window of 500 ms or 250 ms.

Dynamical complexity of population activity

The complexity of population activity was examined in both radiated and PE slices, indicative of the number of factors required to capture the neuronal data[23,24,25,26]. The complexity of radiated slices was higher than controls across all doses of radiation delivered to PFC (Fig. 5A). Complexity was significantly higher than controls for 20 Gy ($p = 1.0116e{-}15$), 50 Gy ($p = 3.316e{-}20$), and 100 Gy ($p1.0041e{-}17$). Thus, radiation reliably increased the complexity of neural data recorded on the hd-MEA

This result was compared to the effect of PE treatment. Relative to baseline activity, slices treated with PE yielded a marked increase in complexity ($p = 4.6426e{-}38$) (Fig. 5B). The magnitude of this effect exceeded the complexity of radiated slices, suggesting that while radiation increased the complexity of neural activity, this effect was limited compared to the high complexity obtained from epileptiform activity, thus showing that population activity following radiation is distinct from a regime of PE-induced seizures. Eigenvalue distributions across experimental conditions further supported this point. In controls and radiated slices, a limited number of eigenvalues yielded positive values; by comparison, PE activity was characterized by a broad distribution of eigenvalues spanning at least two orders of magnitude (Fig. 5C).

Together, the above results on firing rates, functional connectivity, and complexity show clear distinctions between epileptiform and radiation-induced changes in neuronal activity across populations of cortical cells. While both forms of activity were characterized by an increase in firing rates, radiated slices exhibited different patterns of functional connectivity and lower complexity than PE-treated slices.

Quantifying cell death following radiation

A subset of slices was stained with PI following radiation or sham radiation (control) conditions (Fig. 6A). The mean pixel intensity across radiation conditions revealed a trend whereby higher doses resulted in a higher level of cell death (Fig. 6B). In this way, 20 Gy yielded higher intensity than controls ($p = 1.8954e{-}10$), 50 Gy was above 20 Gy ($p = 4.1943e{-}12$), and 100 Gy above 50 Gy ($p = 2.426e{-}12$). Thus, cell death was linked to the radiation dose delivered to PFC neurons. At higher doses, particularly 100 Gy, we observed a clustered spatial arrangement of pixels with higher intensity, suggesting an area where cellular damage was more pronounced (Fig. 6A, arrow). Interestingly, this area is in the vicinity of the secondary motor area (M2), a region known to yield increased cell death following radiation[27,28]. Limitations of the hd-MEA chips, however, did not allow us to record activity from slices after imaging, hence it remains an open question whether these areas displayed aberrant neuronal activity.

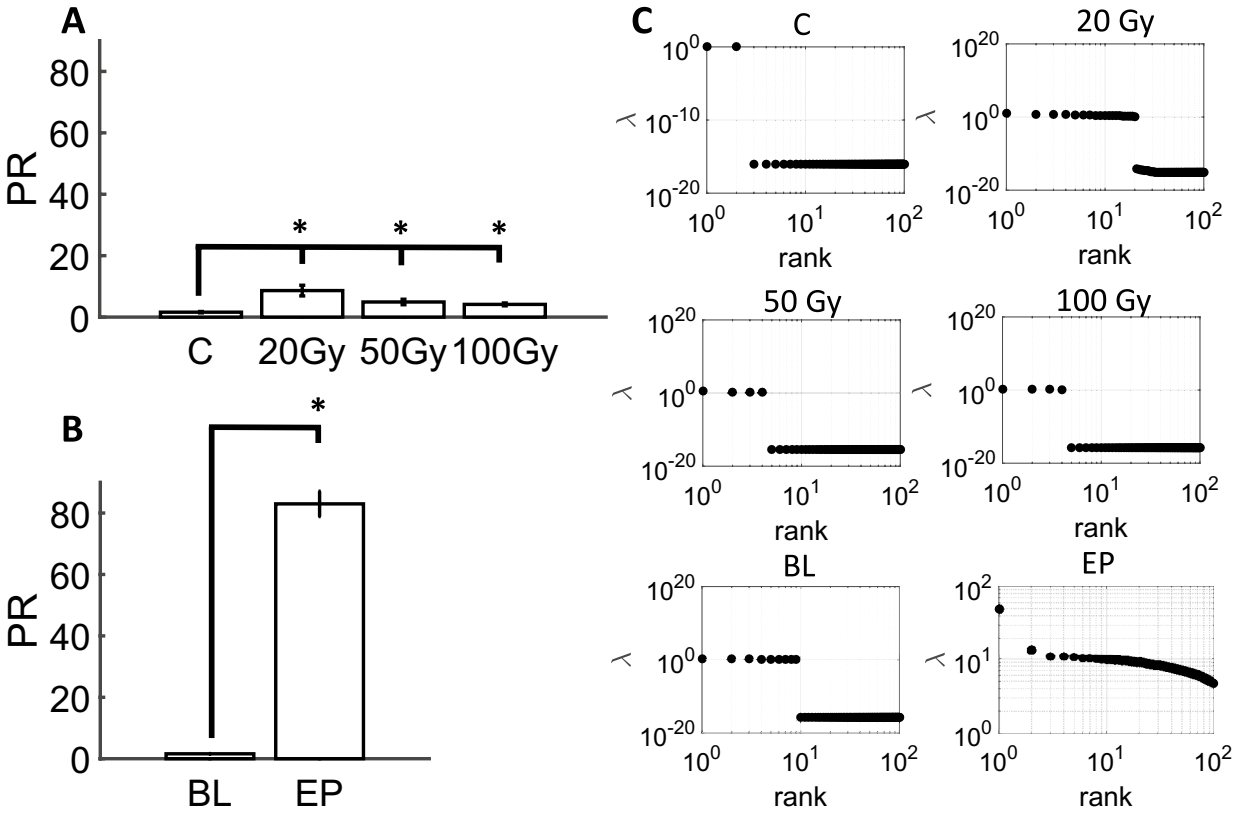

Fig. 5. Neuronal complexity of cortical networks. Participation ratio (PR) in radiated slices (**A**). PR in slices treated with PE solution (**B**). Distribution of eigenvalues across experimental conditions (**C**).

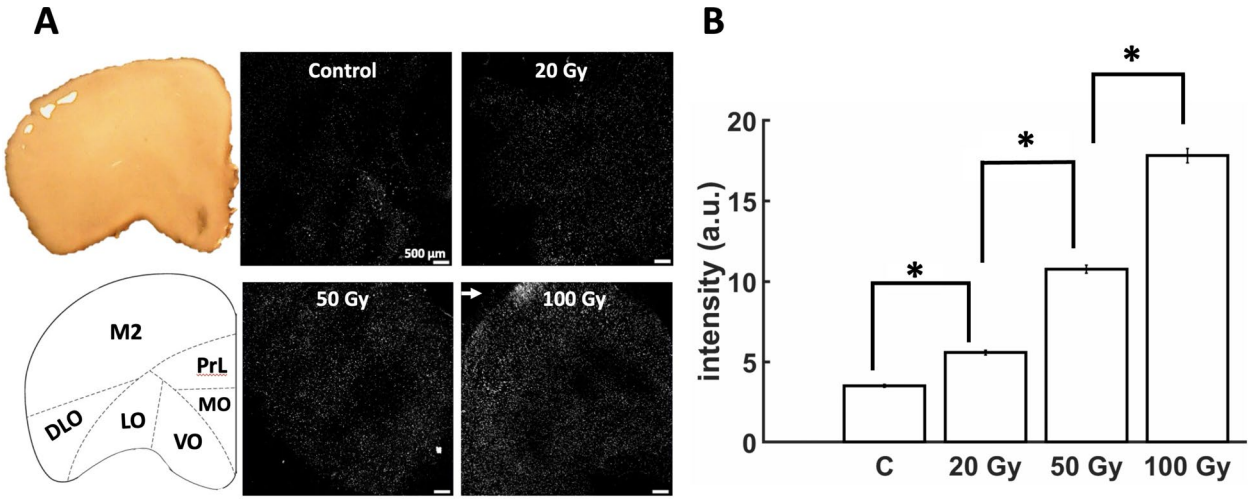

Fig. 6. Propidium iodide (PI) staining of prefrontal slices following radiation. (**A**) Representative samples showing a graded increase in PI intensity with radiation dose. Arrow shows clustering of PI intensity at 100 Gy. Left panel shows approximate location of secondary motor cortex (M2), Prelimbic cortex (PrL), medial orbital cortex (MO), ventral orbital cortex (VO), lateral orbital cortex (LO), and dorsolateral orbital cortex (DLO), (**B**) Mean PI intensity ("a.u.": arbitrary units).

Discussion

This study aimed to investigate the neuromodulatory effects of radiation on the firing rate, functional connectivity, complexity, and survival of PFC cells, and to compare the results with those obtained during epileptiform activity[29]. We found a marked increase in neuronal activity following acute doses of radiation[2], accompanied by an increase in complexity, as well as in the density and in some cases the strength of functional connectivity. Graph theoretic measures of functional connectivity including global efficiency, assortativity, and transitivity were preferentially altered in radiated networks. Global synchronization was increased in high doses of radiation (100 Gy). Finally, radiation induced a dose-dependent cell death where damage was selectively localized to areas surrounding M2, a region particularly vulnerable to radiation damage[27,28].

These results were distinct from epileptiform activity, where complexity was markedly higher, and functional connections were strong but exhibited a lower density than radiated slices due to the restricted spatial focus of epileptic seizures. Differences between radiated slices and epileptiform activity highlight clear distinctions between the effects obtained in these two conditions: while neuronal activity and complexity were elevated in both radiated and PE slices, functional connections were more widely spread in radiation than under PE treatment. This work proposes a novel assay to test the impact of clinically relevant doses of radiation[15,16] on neural dynamics and cellular apoptosis.

Past research has established that firing rate and cross-correlations can increase together[30] making it difficult to separate the two. However, it is worth noting that these two markers do not always increase together. For instance, during epileptiform activity, firing rates and the mean strength correlations are elevated compared to radiated slices, yet the density of functional connections was markedly lower. This is explained by the fact that waves of epileptiform activity occupied a spatially delimited region of the array (Fig. 2B)[17]. In cortical networks, correlations are modulated by a balance of excitatory and inhibitory synaptic transmission, making them an intricate marker of activity across broad populations of neurons[31].

Our findings outlined a marked increase in complexity during epileptiform activity, compared to a more moderate increase in radiated slices relative to controls. These findings can be understood in the following way. The activity recorded from large groups of neurons exhibits a high degree of redundancy due to the covariation across many neurons[32]. Because of this redundancy, neural activity occupies a small area of dynamical space relative to the total number of activity patterns that could be produced, analogous to consistently rolling a "1" or "2" with a six-sided dice. The PR aims to measure the size of the area occupied by neural activity, technically known as the dimensionality of the manifold. This dimensionality reflects the degrees of freedom required to capture the covariation across neurons[23,25,33,34]. If a single eigenvalue is sufficient to explain all of the variance in activity, the PR will yield a value of 1. Conversely, if many eigenvalues are required, the PR will approach a value corresponding to the number of neurons recorded. Our results indicate that both EP and radiation broadens the manifold of activity, resulting in less repeatable patterns over time.

The effects of radiation on neural dynamics within PFC networks remain to be fully elucidated, with past literature showing increased firing rates[2], changes in synaptic morphology[2,7], inhibited synaptic function and disruptions in synaptic plasticity[4,8]. To date, however, scant attention has been devoted to intra- or inter-areal functional connectivity. Further, much of the literature has focused on the effect of radiation on the hippocampus, leaving a growing need to study the PFC due to its involvement in the hippocampal-PFC pathway. This pathway is believed to play a key role in the cognitive deficits/impairments experienced following radiation[2,27,35,36]. Moreover, the PFC has been identified as one of the areas that are most sensitive to radiation[27,36,37].

Given established links between functional connectivity and cognitive outcomes[19, 20, 38], examining the effects of radiation on functional connectivity in reduced hd-MEA preparations is of critical importance to understanding the neurophysiological mechanisms of radiation-induced damage and their impact in clinical settings. Our findings of a dose-dependent disruption in functional connectivity are aligned with human imaging studies showing altered functional connectivity among regions that receive radiation[35, 39, 40, 41]. In turn, higher doses of radiation are associated with worse long-term cognitive prognoses[5]. Understanding the cellular origins of functional connectivity in healthy and radiated brain circuits provides a fruitful avenue to develop interventions that limit radiation-induced cognitive damage.

Because the current study focused on the acute effects of radiation, the timescale of alterations in activity and functional connectivity following radiation remains limited. In-vitro acute brain slices under standard experimental conditions have a typical lifespan of 6–12 h[42]. As a result, this study was limited to a window of only a few hours post-radiation and could not examine early delayed or late delayed radiation-induced injuries[3, 4]. Despite this limitation, it is reasonable to assume that a majority of the injuries induced by radiosurgery are acute in nature given that extremely high doses are delivered within a brief time period. These findings are also consistent with previous investigations of the acute effects of radiation on PFC neurons[2]. Further research on early and late delayed radiation-induced injuries suggests differential effects based on the timescale following radiation whereby an initial increase in firing rate is eventually followed by a decrease in activity[2, 6]. Similar results have been reported in human nasopharyngeal carcinoma patients[43], showing an acute increase in local activity which was associated with a decrease in functional connections and higher levels of necrosis in the late-delayed stage.

Further work will be needed to investigate the intracellular mechanisms involved in radiation-induced alterations in neuronal activity, functional connectivity, and cellular apoptosis, as hd-MEAs are restricted to tracking extracellular voltage deflections in the vicinity of cells. For example, ionic channel kinetics or patch clamp experiments may prove fruitful in determining why PFC neurons become hyperexcitable as these mechanisms are not accessible via hd-MEA recordings. Past research has shown acute downregulation in excitatory NR2A subunits of the N-methyl-D-aspartate receptors (NMDAR) and increases in inhibitory gamma-aminobutyric acid receptors ($GABA_A$Rs), leading to changes in synaptic function and inhibiting long-term potentiation[8]. It is unclear how these phenomena are linked to broader effects on neuronal networks such as alterations in the density and strength of functional connections. Simultaneous intra/extracellular recordings, though technically difficult, may offer insights in this regard[44, 45].

Given that hd-MEAs revealed markers of radiation-induced damage in neuronal activity and network interactions, it would be beneficial to examine the potential impact of pharmacological preconditioning in preventing these alterations. Past research has shown that pre-treating brain slices with memantine, an NMDAR antagonist[8] or administering oral doses of epigallocatechin-3-gallate (EGCG), the main polyphenolic compound in green tea[46], and Quercetin, a flavonoid that is found in several vegetables and fruits[47], can provide neuroprotective effects against radiation damage.

One limitation of hd-MEA recordings is that it is not logistically possible to deliver fractionated doses of radiation that are used in typical radiation therapy protocols. Although implantable in vivo arrays are available, there are significant concerns regarding the radiosensitivity of the hd-MEA platform. In addition, the use of anaesthetics during in vivo protocols is known to influence brain activity and alter neuronal functioning[48, 49], which may impact recordings. We opted for large single doses of radiation such as those used for stereotactic radiosurgery, pulsed high-dose-rate brachytherapy and certain hypofractionated palliative treatment protocols[15, 16, 50]. These doses also provided a benchmark to compare the effects of standard dose rates (5–10 Gy/min) to ultrafast dose rates (> 40 Gy/s) on various markers of neural activity and cell death.

Alternate dose ranges such as those below 20 Gy or above 100 Gy could be employed in future studies to determine whether the same neural dynamics and dose-dependent cellular apoptosis would be observed. Notably, doses above 60 Gy have been shown to produce radiation-induced necrosis (radionecrosis) and lesions in animal models[6, 51]; however, clinical studies have revealed radionecrosis in normal tissues exposed to doses as low as 12 Gy[52, 53, 54]. Similar to these findings, our results revealed that cell death occurred in a dose-dependent manner beginning at doses as low as 20 Gy. Finally, future studies should examine different regions of the brain using the methods employed in this study to determine whether there are area-specific impacts of these doses.

In conclusion, hd-MEAs revealed radiation-induced changes in broad networks of the PFC that were characterized by increased firing rates, higher complexity, disrupted functional connectivity, and dose-dependent apoptosis. These markers were distinct from those observed in hd-MEA recordings of epileptiform activity, thus showing that radiation does not merely induce an epileptic state. These results point to hd-MEAs as a novel and promising tool for studying the interactions of clinically relevant doses of radiation and potential targets for radioprotection.

Methods

Overview of electrophysiological data Collection

A total of 12 acute PFC slices were assigned to either the pro-epileptiform (PE, 2 slices) or radiation (10 slices) treatment (Fig. 7). This number is common for hd-MEA recordings as the statistical sample size is determined by the number of electrodes ($n = 4{,}096$) that are simultaneously recorded rather than the total number of slices. Fewer slices were analyzed for the pro-epileptiform treatment given that widespread ictal events constitute rare occurrences and were obtained from a previously published data set[17]. Slices receiving the PE treatment were first recorded at baseline using the hd-MEA, then perfused with the PE solution and recorded again after 20 min. Slices receiving the radiation treatment were split into control (4 slices) and radiated (6 slices) groups. Escalating radiation doses of 20 Gy, 50 Gy and 100 Gy were delivered to each of the slices followed by a 45-minute recovery period. These slices were then either recorded on the hd-MEA or imaged using propidium iodide (PI) staining.

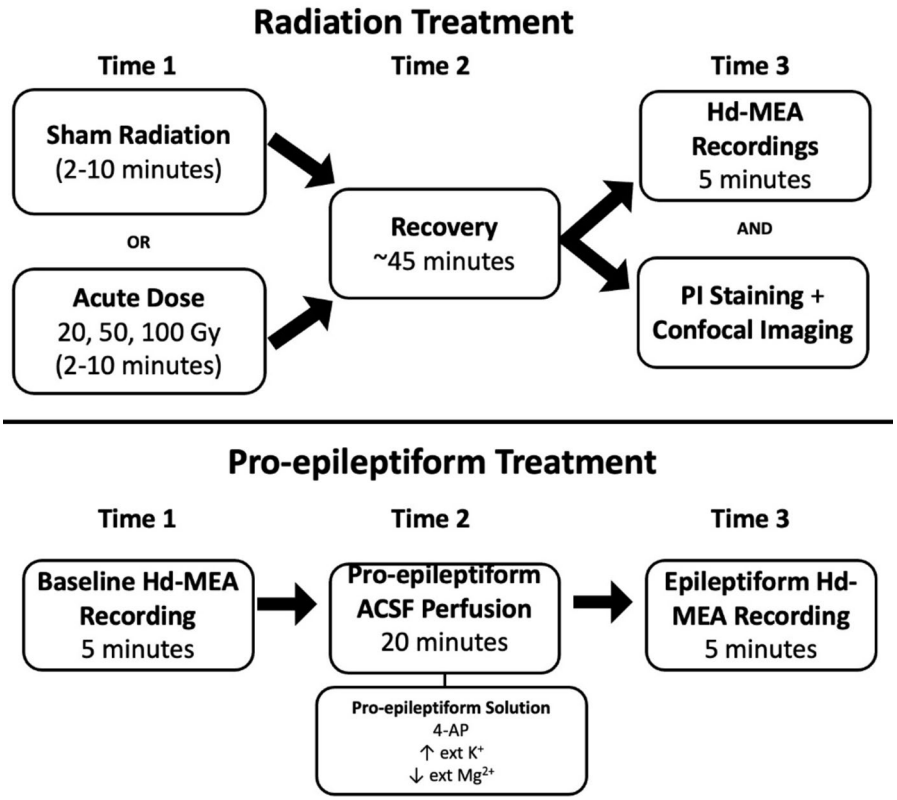

Fig. 7. Illustration of the protocol employed to perform radiation, record neural activity, and apply PI staining to prefrontal cortical slices. A comparison of activity under radiation and PE treatment was performed.

Control slices received sham radiation followed by 45 min of recovery before proceeding to the recording or imaging step. Together, this platform provides a direct comparison between epileptiform- and radiation-induced changes in neural activity, as well as an evaluation of dose-dependent apoptosis.

Animals

Data were collected using Sprague Dawley rats of both sexes, aged 14–21 days, purchased from Charles River. We chose to study juvenile animals as past research has shown that brain slices from juveniles attain higher survival rates than later developmental stages[55]. The neurons in juvenile slices are also generally more resistant to various insults when compared to adult animals, suggesting that the effects reported in the juvenile slices may be even greater in mature animals[56]. Another motivating factor for studying juvenile rodents comes from age-dependent findings in human patients. Past research has shown an age-dependent effect of radiation whereby younger patients typically experience poorer outcomes than adult patients, thus highlighting the importance of studying these effects[57]. These findings have also been replicated in rodent studies[4].

Animals were housed in standard housing conditions with cage enrichment and ad libitum access to water and standard chow. All experiments were carried out in accordance with Canadian Council on Animal Care Guidelines. All procedures were approved by the University of Ottawa Animal Care and Veterinary Services and comply with the ARRIVE guidelines.

Acute slice preparation

Animals were deeply anaesthetized using isoflurane (Baxter Corporation) and were subsequently euthanized via decapitation. The brains of the animals were quickly extracted and submerged into a frozen choline dissection buffer. The buffer consisted of the following: 119.0 mM choline chloride, 2.5 mM KCl, 4.3 mM $MgSO_4$, 1.0 mM $CaCl_2$, 1.0 mM NaH_2PO_4, 1.3 mM sodium ascorbate, 11.0 mM glucose, 26.2 mM NaHCO3, and was perfused with carbogen (95% O_2/5% CO_2) for 25 min prior to performing the dissection. The brains were sliced coronally at a thickness of 300 µm using a Leica VT1000S vibratome. Acute slices containing the PFC were used for all experiments. Due to the technological limitations of hd-MEA experiments, we were limited to performing a crude identification of the anatomical regions located within our slices. Given that we were unable to determine the exact anatomical localization of the slices, our goal was to understand the impact of radiation on PFC networks more broadly rather than provide localized effects of radiation on specific regions of the PFC.

Once the slices were collected, they were placed in a recovery chamber filled with a standard artificial cerebrospinal fluid (ACSF) consisting of the following: 119.0 mM NaCl, 2.5 mM KCl, 1.3 mM $MgSO_4$, 2.5 mM $CaCl_2$, 1.0 mM NaH_2PO_4, 11.0 mM glucose, and 26.2 mM $NaHCO_3$. The ACSF was continuously perfused using carbogen

(95% O_2/5% CO_2) and maintained at a temperature of 37˚C. Following slicing, brain slices were left to recover for 1 h prior to experiments allowing the ACSF to equilibrate to room temperature.

Radiation

Acute doses of radiation consisting of 20 Gy, 50 Gy, or 100 Gy were administered to a subset of healthy slices using the robotic radiosurgery platform (Cyberknife® G4) at a standard dose rate of 10 Gy/min. The use of non-fractionated doses was selected to serve as a stepping stone for comparing standard dose rates to ultra-fast delivery methods such as FLASH radiation. These ultra-fast dose rates are several orders of magnitude greater than those used in conventional RT and have shown promise in maintaining the efficacy of the treatment while reducing radiation-induced injuries[58, 59, 60, 61, 62]. While acute PFC brain slices were continuously perfused with carbogen (95% O_2/5% CO_2) throughout the experiment, perfusion was temporarily halted while radiation doses were administered (2–10 min depending on the dose). The radiation beam was 60 mm in diameter and slices were placed in the center of the beam to ensure a homogeneous dose across the entire brain slice. Control slices were brought over to the same location as the Cyberknife to control for potential mechanical damage during transport. In addition, the carbogen perfusion was temporarily stopped for ~ 2–10 min to mimic the experimental conditions. However, no radiation was delivered to these slices. Distinct slices were employed for radiation and controls given that hd-MEAs could not be radiated due to potential damage to the chips. The slices in both conditions were then employed to either record neural activity or were stained with PI to quantify cell death.

Epileptiform activity

We used a pro-epileptiform ACSF (PE-ACSF) containing the following: 120 mM NaCl, 8.5 mM KCl,1.25 mM NaH2PO4, 0.25 mM MgSO4, 2 mM CaCl2, 24 mM NaHCO3, 10 mM dextrose, and 0.05 mM 4-AP to generate interictal-like neural activity[29]. In this condition, baseline recordings were taken from the same slices prior to the application of PE-ACSF. Following baseline recordings, slices were perfused in PE-ACSF for 20 min and 10-minute recordings of neural activity were collected. The baseline slices differ slightly from the radiation control slices in that they were not exposed to the same potential mechanical damage caused by transporting the slices to be irradiated.

Hd-MEA recordings

System Description. Recordings of network-level neural activity were collected using an active pixel sensor hd-MEA. This hd-MEA used a CMOS-based CCD monolithic chip in which the pixels were modified to detect changes in electric voltages from electrogenic tissues. The array provided simultaneous recordings from 4,096 electrodes with a sampling frequency of 18 kHz across the entire array. The hd-MEA chips were comprised of 64 × 64 electrodes arranged as a pixel element array whereby each pixel measures 21 x 21 m with an electrode pitch of 42 m. The active area of the array was 7.22 mm^2 and had a pixel density of 567 pixels/mm^2[14, 63]. Data were acquired using BrainWave software (*3Brain Gmbh*, *Switzerland*) and imported to MATLAB (MathWorks, Natick) for offline analysis.

Hd-MEA Recording Protocol. A subset of acute PFC slices from each condition were placed on the hd-MEA chip, held in place by a harp and bathed in standard ACSF that was continuously perfused with carbogen (95% O_2/5% CO_2). Slices were maintained at a temperature of 37 °C throughout the recording period. Recordings were completed in a dark environment to prevent interference from light artefacts. Five minutes of neural activity was recorded from each slice.

Quantifying Cell Death in Irradiated Brain Slices. A different subset of brain slices (4 slices) from each dose condition (20, 50, and 100 Gy) and the control condition were subsequently stained using PI (1 mg/mL, Sigma–Aldrich), a cell death marker that binds to the DNA of neurons with fragmented plasma membranes but remains membrane impermeable in healthy neurons[64]. Following a 15-minute application of PI, serial dilution of the PI-stained ACSF was performed and acute brain slices were imaged using a Zeiss LSM880 confocal microscope. We quantified cell death based on the mean intensity of images taken from PI-stained slices.

Data Preparation. Data collected from all conditions were initially processed using a second-order bandpass Butterworth filter in the forward and reverse directions (300-5000 Hz) applied to the raw voltages to remove high-frequency noise and slowly changing field potentials[65]. Artefacts were identified as any timepoint where the voltages were greater than 1000 μV. Artefacts were subsequently replaced with the mean of the filtered data. Spike times were then extracted based on their multi-unit activity (MUA) using a voltage-threshold method[66] whereby we identified negative signal peaks below a threshold of 5 standard deviations (SD) from the mean of the filtered signal. To determine our final threshold, we first calculated the mean and SD of the filtered baseline data and then took the difference between the two as our overall threshold. This final threshold was then applied to voltage data to identify multi-unit spike times, representing the activity of neurons within the vicinity of individual channels on the hd-MEA. A sample of the data and a MATLAB tutorial script is available as Supplementary Material.

A known limitation associated with MUAs is the possibility of capturing signal redundancies whereby a single channel picks up the activity from multiple neurons or a single neuron's activity is picked up by multiple channels on the array[67, 68, 69]. Consequently, this method lacks the ground truth necessary to provide single-neuron resolution data. Despite this, broadband signals can be split into slower components (< 100 Hz) that represent local field potentials and faster components (300–5000 Hz) that constitute MUA or the sum of activity of the neurons in the vicinity of a single electrode[70, 71, 72, 73, 74]. While inferential methods can be employed to sort the MUA into putative single-cell contributions[67, 68, 69], a ground truth comparison is required to provide accurate spike sorting. Even in the absence of direct ground truth validation, studies have shown that MUAs capture key properties of activity in neural circuits and can be used to adequately infer firing rates and correlations amongst neurons[75].

Neuronal Spike Rates. Spike times were employed to generate rasters that represent the activity of entire networks across time. Rasters were downsampled from 18 kHz to 1 kHz using non-overlapping temporal bins of binary data set to "1" in the presence of one or more spikes, or "0" if no spikes were present. We then computed a peri-stimulus time histogram using a rolling temporal window. A broad window of 500 ms was used as spike rates were low. Channels without activity were removed from further analyses. Firing rates were assessed using a Kolmogorov-Smirnov test of normality which revealed non-normal distributions for all conditions ($p < 0.001$). Past research has also established that cortical firing rate distributions follow a log-normal distribution rather than a normal distribution[76,77]. As such, we opted to compare firing rates (Hz) using a non-parametric Wilcoxon rank sum test (significance level: $p = 0.01$), which assumes independence across samples but relaxes the assumption of Gaussian normality[78]. Finally, the use of a non-parametric test on global data distributions ensured that we did not overemphasize any minor effects that may have been amplified given the substantial number of channels ($n = 4{,}096$) that were simultaneously recorded via the hd-MEA.

Functional Connectivity. Data were downsampled from 18 kHz to 1 kHz and a rolling window of 10 ms was applied prior to computing Pearson correlations. Pearson cross-correlations were computed for each pair of electrodes within the hd-MEA, yielding a $4{,}096 \times 4{,}096$ matrix of interactions. These correlations were subsequently passed through a threshold of $r = 0.2$ to detect the presence or absence of a functional connection between pairs of channels, representing the statistical coincidence of multi-unit spikes at these channels. Data were assessed for normality using a Kolmogorov-Smirnov test followed by a Wilcoxon rank sum test.

Neural Complexity. Spatiotemporal patterns of activity recorded on the hd-MEA were described by their participation ratio (PR), a measure of neural complexity reflecting the number of factors needed to capture fluctuations in the data[23,25,33,34]. The PR of population recordings was computed by first extracting 10 brief time segments of data (mean duration: 3,811.5 ms, SEM: 145.17) across each experimental condition. The PR of each segment was computed by eigenspectrum decomposition[79], providing ranked eigenvalues $\lambda_1, \ldots, \lambda_N$ where N denotes the total number of channels on the hd-MEA. Then, the PR was calculated as the first moment of the eigenspectrum normalized by the second moment,

$$\mathrm{PR} = \frac{\left(\sum_i^N \lambda_i\right)^2}{\sum_i^N \lambda_i^2}. \tag{1}$$

If patterns of population activity can be described by a limited number of dimensions, only a portion of eigenvalues will be positive, resulting in a low PR. However, patterns of activity with higher complexity would yield a large number of positive eigenvalues and hence a higher PR.

Data availability

The data described in this study will be made available upon reasonable request to the corresponding author (J.P. Thivierge, jthivier@uottawa.ca). A Matlab tutorial (dx.doi.org/10.6084/m9.figshare.26789953) and sample data (dx.doi.org/10.6084/m9.figshare.26597269) are available online as a free resource.

Received: 11 June 2024; Accepted: 23 August 2024
Published online: 29 August 2024

References

1. Quigg, M., Rolston, J. & Barbaro, N. M. Radiosurgery for epilepsy: Clinical experience and potential antiepileptic mechanisms. *Epilepsia* **53**(1), 7–15. https://doi.org/10.1111/j.1528-1167.2011.03339.x (2012).
2. Zhang, D. *et al.* Cranial irradiation induces axon initial segment dysfunction and neuronal injury in the prefrontal cortex and impairs hippocampal coupling. *Neuro-Oncol Adv.* **2**(1), vdaa058. https://doi.org/10.1093/noajnl/vdaa058 (2020).
3. Greene-Schloesser, D. *et al.* Radiation-induced brain injury: A review. *Front. Oncol.* **2**, 73 (2012).
4. Zhang, D. *et al.* Radiation induces age-dependent deficits in cortical synaptic plasticity. *Neuro-Oncol* **20**(9), 1207–1214. https://doi.org/10.1093/neuonc/noy052 (2018).
5. Brière, M. E., Scott, J. G., McNall-Knapp, R. Y. & Adams, R. L. Cognitive outcome in pediatric brain tumor survivors: Delayed attention deficit at long-term follow-up. *Pediatr. Blood Cancer* **50**(2), 337–340. https://doi.org/10.1002/pbc.21223 (2008).
6. Zaer, H. *et al.* Non-ablative doses of focal ionizing radiation alters function of central neural circuits. *Brain Stimulat.* **15**(3), 586–597. https://doi.org/10.1016/j.brs.2022.04.001 (2022).
7. Kempf, S. J. *et al.* Neonatal irradiation leads to persistent proteome alterations involved in synaptic plasticity in the mouse hippocampus and cortex. *J. Proteome Res.* **14**(11), 4674–4686. https://doi.org/10.1021/acs.jproteome.5b00564 (2015).
8. Wu, P. *et al.* Radiation induces acute alterations in neuronal function. *PLOS ONE* **7**(5), e37677. https://doi.org/10.1371/journal.pone.0037677 (2012).
9. Carlén, M. What constitutes the prefrontal cortex?. *Science* **358**(6362), 478–482. https://doi.org/10.1126/science.aan8868 (2017).
10. Miller, E. K. & Cohen, J. D. An integrative theory of prefrontal cortex function. *Annu. Rev. Neurosci.* **24**(1), 167–202. https://doi.org/10.1146/annurev.neuro.24.1.167 (2001).
11. Thierry, A. M., Gioanni, Y., Dégénétais, E. & Glowinski, J. Hippocampo-prefrontal cortex pathway: Anatomical and electrophysiological characteristics. *Hippocampus* **10**(4), 411–419. https://doi.org/10.1002/1098-1063(2000)10:4<411::AID-HIPO7>3.0.CO;2-A (2000).
12. Gould, J. Breaking down the epidemiology of brain cancer. *Nature* **561**(7724), S40–S41. https://doi.org/10.1038/d41586-018-06704-7 (2018).
13. Stevenson, I. H. & Kording, K. P. How advances in neural recording affect data analysis. *Nat. Neurosci.* **14**(2), 2. https://doi.org/10.1038/nn.2731 (2011).
14. Ferrea, E. *et al.* Large-scale, high-resolution electrophysiological imaging of field potentials in brain slices with microelectronic multielectrode arrays. *Front. Neural Circ.* **6**, 80 (2012).
15. Redmond, K. J. *et al.* Tumor control probability of radiosurgery and fractionated stereotactic radiosurgery for brain metastases. *Int. J. Radiat. Oncol.* **110**(1), 53–67. https://doi.org/10.1016/j.ijrobp.2020.10.034 (2021).
16. Tuleasca, C., Vermandel, M. & Reyns, N. Stereotactic radiosurgery: From a prescribed physical radiation dose toward biologically effective dose. *Mayo Clin. Proc.* **96**(5), 1114–1116. https://doi.org/10.1016/j.mayocp.2021.03.027 (2021).

17. Boucher-Routhier, M. & Thivierge, J. P. A deep generative adversarial network capturing complex spiral waves in disinhibited circuits of the cerebral cortex. *BMC Neurosci.* **24**(1), 22. https://doi.org/10.1186/s12868-023-00792-6 (2023).
18. Craddock, R. C., Holtzheimer, P. E. III, Hu, X. P. & Mayberg, H. S. Disease state prediction from resting state functional connectivity. *Magn. Reson. Med.***62** (6), 1619–1628. https://doi.org/10.1002/mrm.22159 (2009).
19. Konstantinou, N., Pettemeridou, E., Stamatakis, E. A., Seimenis, I. & Constantinidou, F. Altered resting functional connectivity is related to cognitive outcome in males with moderate-severe traumatic brain injury. *Front. Neurol.* **9**, 1163. https://doi.org/10.3389/fneur.2018.01163 (2019).
20. Lang S et al. (2017) Functional connectivity in frontoparietal network: Indicator of preoperative cognitive function and cognitive outcome following surgery in patients with glioma. *World Neurosurg.***105**, 913–922. https://doi.org/10.1016/j.wneu.2017.05.149
21. Wang, K. *et al.* Altered functional connectivity in early Alzheimer's disease: A resting-state fMRI study. *Hum. Brain Mapp.* **28**(10), 967–978. https://doi.org/10.1002/hbm.20324 (2007).
22. Rubinov, M. & Sporns, O. Complex network measures of brain connectivity: Uses and interpretations. *NeuroImage* **52**(3), 1059–1069. https://doi.org/10.1016/j.neuroimage.2009.10.003 (2010).
23. Altan, E., Solla, S. A., Miller, L. E. & Perreault, E. J. Estimating the dimensionality of the manifold underlying multi-electrode neural recordings. *PLOS Comput. Biol.* **17**(11), e1008591. https://doi.org/10.1371/journal.pcbi.1008591 (2021).
24. Hu, Y. & Sompolinsky, H. The spectrum of covariance matrices of randomly connected recurrent neuronal networks, p. 24, (2020).
25. Litwin-Kumar, A., Harris, K. D., Axel, R., Sompolinsky, H. & Abbott, L. F. Optimal degrees of synaptic connectivity. *Neuron* **93**(5), 1153–1164. https://doi.org/10.1016/j.neuron.2017.01.030 (2017) (.**e7**).
26. Mazzucato, L., Fontanini, A. & Camera, G. L. Stimuli reduce the dimensionality of cortical activity. *Front. Syst. Neurosci.* **10**, 11. https://doi.org/10.3389/fnsys.2016.00011 (2016).
27. Hnilicová, P. *et al.* Anatomic and metabolic alterations in the rodent frontal cortex caused by clinically relevant fractionated whole-brain irradiation. *Neurochem Int.* **154**, 105293. https://doi.org/10.1016/j.neuint.2022.105293 (2022).
28. Ueno, H. *et al.* Region-specific reduction of parvalbumin neurons and behavioral changes in adult mice following single exposure to cranial irradiation. *Int. J. Radiat. Biol.* **95**(5), 611–625. https://doi.org/10.1080/09553002.2019.1564081 (2019).
29. Postnikova, T. Y., Amakhin, D. V., Trofimova, A. M. & Zaitsev, A. V. Calcium-permeable AMPA receptors are essential to the synaptic plasticity induced by epileptiform activity in rat hippocampal slices. *Biochem. Biophys. Res. Commun.* **529**(4), 1145–1150. https://doi.org/10.1016/j.bbrc.2020.06.121 (2020).
30. de la Rocha, J., Doiron, B., Shea-Brown, E., Josić, K. & Reyes, A. Correlation between neural spike trains increases with firing rate. *Nature* **448**(7155), 802–806. https://doi.org/10.1038/nature06028 (2007).
31. Mazzoni, A. *et al.* On the dynamics of the spontaneous activity in neuronal networks. *PLOS ONE* **2**(5), e439. https://doi.org/10.1371/journal.pone.0000439 (2007).
32. Cunningham, J. P. & Yu, B. M. Dimensionality reduction for large-scale neural recordings. *Nat. Neurosci.* **17**(11), 1500–1510. https://doi.org/10.1038/nn.3776 (2014).
33. Mazzucato, L., Fontanini, A. & Camera, G. L. Stimuli reduce the dimensionality of cortical activity. *Front. Syst. Neurosci.* **10**(11), 11. https://doi.org/10.3389/fnsys.2016.00011 (2016).
34. Hu, Y. & Sompolinsky, H. The spectrum of covariance matrices of randomly connected recurrent neuronal networks with linear dynamics. *PLoS Comput. Biol.* **18**, e1010327. https://doi.org/10.1371/journal.pcbi.1010327 (2022).
35. , S. C. *et al.* Prognosis of hippocampal function after sub-lethal irradiation brain injury in patients with nasopharyngeal carcinoma. *Sci. Rep.* **7**(1), 14697 (2017). https://doi.org/10.1038/s41598-017-13972-2.
36. Kovalchuk, A. & Kolb, B. Low dose radiation effects on the brain–from mechanisms and behavioral outcomes to mitigation strategies. *Cell Cycle* **16**(13), 1266–1270 (2017).
37. Kornev, M. A., Kulikova, E. A. & Kul'bakh, O. S. The cellular composition of the cerebral cortex of rat fetuses after fractionated low-dose irradiation. *Neurosci. Behav. Physiol.* **35**(6), 635–638. https://doi.org/10.1007/s11055-005-0104-3 (2005).
38. Hawellek, D. J., Hipp, J. F., Lewis, C. M., Corbetta, M. & Engel, A. K. Increased functional connectivity indicates the severity of cognitive impairment in multiple sclerosis. *Proc. Natl. Acad. Sci.* **108**(47), 19066–19071. https://doi.org/10.1073/pnas.1110024108 (2011).
39. Kovács, Á. *et al.* Changes in functional MRI signals after 3D based radiotherapy of glioblastoma multiforme. *J. Neurooncol* **125**(1), 157–166. https://doi.org/10.1007/s11060-015-1882-2 (2015).
40. Ma, Q. *et al.* Radiation-induced functional connectivity alterations in nasopharyngeal carcinoma patients with radiotherapy. *Med. (Baltim).* **95**(29), e4275. https://doi.org/10.1097/MD.0000000000004275 (2016).
41. Mitchell, T. J. *et al.* Human brain functional network organization is disrupted after whole-brain radiation therapy. *Brain Connect.* **10**(1), 29–38. https://doi.org/10.1089/brain.2019.0713 (2020).
42. Buskila, Y. *et al.* Extending the viability of acute brain slices. *Sci. Rep.* **4**(4), 4. https://doi.org/10.1038/srep05309 (2014).
43. Ding, Z. *et al.* Radiation-induced brain structural and functional abnormalities in presymptomatic phase and outcome prediction. *Hum. Brain Mapp.* **39**(1), 407–427. https://doi.org/10.1002/hbm.23852 (2018).
44. Dipalo, M. *et al.* Intracellular and extracellular recording of spontaneous action potentials in mammalian neurons and cardiac cells with 3D plasmonic nanoelectrodes. *Nano Lett.* **17**(6), 3932–3939. https://doi.org/10.1021/acs.nanolett.7b01523 (2017).
45. Hamilton, F., Berry, T. & Sauer, T. Tracking intracellular dynamics through extracellular measurements. *PLOS ONE* **13**(10), e0205031. https://doi.org/10.1371/journal.pone.0205031 (2018).
46. El-Missiry, M. A., Othman, A. I., El-Sawy, M. R. & Lebede, M. F. Neuroprotective effect of epigallocatechin-3-gallate (EGCG) on radiation-induced damage and apoptosis in the rat hippocampus. *Int. J. Radiat. Biol.* **94**(9), 798–808. https://doi.org/10.1080/09553002.2018.1492755 (2018).
47. Kale, A. *et al.* Neuroprotective effects of Quercetin on radiation-induced brain injury in rats. *J. Radiat. Res. (Tokyo)* **59**(4), 404–410. https://doi.org/10.1093/jrr/rry032 (2018).
48. Huang, Z. *et al.* Altered temporal variance and neural synchronization of spontaneous brain activity in anesthesia. *Hum. Brain Mapp.* **35**(11), 5368–5378. https://doi.org/10.1002/hbm.22556 (2014).
49. Sorrenti, V. *et al.* Understanding the effects of anesthesia on cortical electrophysiological recordings: A scoping review. *Int. J. Mol. Sci.* **22**(3), 3. https://doi.org/10.3390/ijms22031286 (2021).
50. Yuan, H. *et al.* Effects of fractionated radiation on the brain vasculature in a murine model: Blood–brain barrier permeability, astrocyte proliferation, and ultrastructural changes. *Int. J. Radiat. Oncol.* **66**(3), 860–866. https://doi.org/10.1016/j.ijrobp.2006.06.043 (2006).
51. Zaer, H. *et al.* Radionecrosis and cellular changes in small volume stereotactic brain radiosurgery in a porcine model. *Sci. Rep.* **10**(1), 16223. https://doi.org/10.1038/s41598-020-72876-w (2020).
52. Blonigen, B. J. *et al.* Irradiated volume as a predictor of brain radionecrosis after linear accelerator stereotactic radiosurgery. *Int. J. Radiat. Oncol.* **77**(4), 996–1001. https://doi.org/10.1016/j.ijrobp.2009.06.006 (2010).
53. Korytko, T. *et al.* 12 Gy gamma knife radiosurgical volume is a predictor for radiation necrosis in non-AVM intracranial tumors. *Int. J. Radiat. Oncol.* **64**(2), 419–424. https://doi.org/10.1016/j.ijrobp.2005.07.980 (2006).
54. Reynolds, T. A., Jensen, A. R., Bellairs, E. E. & Ozer, M. Dose gradient index for stereotactic radiosurgery/radiation therapy. *Int. J. Radiat. Oncol.* **106**(3), 604–611. https://doi.org/10.1016/j.ijrobp.2019.11.408 (2020).
55. Lipton, P. *et al.* Making the best of brain slices: Comparing preparative methods. *J. Neurosci. Methods* **59**(1), 151–156. https://doi.org/10.1016/0165-0270(94)00205-U (1995).

56. Huang, S. & Uusisaari, M. Y. Physiological temperature during brain slicing enhances the quality of acute slice preparations. *Front. Cell. Neurosci.* **7**, 48. https://doi.org/10.3389/fncel.2013.00048 (2013).
57. Mulhern, R. K., Merchant, T. E., Gajjar, A., Reddick, W. E. & Kun, L. E. Late neurocognitive sequelae in survivors of brain tumours in childhood. *Lancet Oncol.* **5**(7), 399–408. https://doi.org/10.1016/S1470-2045(04)01507-4 (2004).
58. Favaudon, V. *et al.* Ultrahigh dose-rate FLASH irradiation increases the differential response between normal and tumor tissue in mice. *Sci. Transl. Med.* **6**(245), 245ra93-245ra93. https://doi.org/10.1126/scitranslmed.3008973 (2014).
59. Hughes, J. R. & Parsons, J. L. FLASH radiotherapy: Current knowledge and future insights using proton-beam therapy. *Int. J. Mol. Sci.* **21**(18), 18. https://doi.org/10.3390/ijms21186492 (2020).
60. Matuszak, N. *et al.* FLASH radiotherapy: An emerging approach in radiation therapy. *Rep. Pract. Oncol. Radiother.* **27**(2), 2. https://doi.org/10.5603/RPOR.a2022.0038 (2022).
61. Montay-Gruel, P. *et al.* Irradiation in a flash: Unique sparing of memory in mice after whole brain irradiation with dose rates above 100Gy/s. *Radiother Oncol.* **124**(3), 365–369. https://doi.org/10.1016/j.radonc.2017.05.003 (2017).
62. Simmons, D. A. *et al.* Reduced cognitive deficits after FLASH irradiation of whole mouse brain are associated with less hippocampal dendritic spine loss and neuroinflammation. *Radiother. Oncol.* **139**, 4–10. https://doi.org/10.1016/j.radonc.2019.06.006 (2019).
63. Imfeld, K. *et al.* Large-scale, high-resolution data acquisition system for extracellular recording of electrophysiological activity. *IEEE Trans. Biomed. Eng.* **55**(8), 2064–2073. https://doi.org/10.1109/TBME.2008.919139 (2008).
64. Kuebler, E. S., Tauskela, J. S., Aylsworth, A., Zhao, X. & Thivierge, J. P. Burst predicting neurons survive an in vitro glutamate injury model of cerebral ischemia. *Sci. Rep.* **5**(1), 1. https://doi.org/10.1038/srep17718 (2015).
65. Bullmann, T. *et al.* Large-scale mapping of axonal arbors using high-density microelectrode arrays. *Front. Cell. Neurosci.* **13**, 404. https://doi.org/10.3389/fncel.2019.00404 (2019).
66. Lewicki, M. S. A review of methods for spike sorting: The detection and classification of neural action potentials. *Netw. Comput. Neural Syst.* **9**(4), R53-77 (1998).
67. Hilgen, G. *et al.* Unsupervised spike sorting for large-scale, high-density multielectrode arrays. *Cell Rep.* **18**(10), 2521–2532. https://doi.org/10.1016/j.celrep.2017.02.038 (2017).
68. Prentice, J. S. *et al.* Fast, scalable, Bayesian spike identification for multi-electrode arrays. *PLOS ONE* **6**(7), e19884. https://doi.org/10.1371/journal.pone.0019884 (2011).
69. Rossant, C. *et al.* Spike sorting for large, dense electrode arrays. *Nat. Neurosci.* **19**(4), 634–641. https://doi.org/10.1038/nn.4268 (2016).
70. Bansal, A. K., Vargas-Irwin, C. E., Truccolo, W. & Donoghue, J. P. Relationships among low-frequency local field potentials, spiking activity, and three-dimensional reach and grasp kinematics in primary motor and ventral premotor cortices. *J. Neurophysiol.* **105**(4), 1603–1619. https://doi.org/10.1152/jn.00532.2010 (2011).
71. Davis, Z. W., Muller, L. & Reynolds, J. H. Spontaneous spiking is governed by broadband fluctuations. *J. Neurosci.* **42**(26), 5159–5172. https://doi.org/10.1523/JNEUROSCI.1899-21.2022 (2022).
72. Legatt, A. D., Arezzo, J. & Vaughan, H. G. Averaged multiple unit activity as an estimate of phasic changes in local neuronal activity: Effects of volume-conducted potentials. *J. Neurosci. Methods* **2**(2), 203–217. https://doi.org/10.1016/0165-0270(80)90061-8 (1980).
73. Mitzdorf, U. Current source-density method and application in cat cerebral cortex: Investigation of evoked potentials and EEG phenomena. *Physiol. Rev.* **65**(1), 37–100. https://doi.org/10.1152/physrev.1985.65.1.37 (1985).
74. Stark, E. & Abeles, M. Predicting movement from multiunit activity. *J. Neurosci.* **27**(31), 8387–8394. https://doi.org/10.1523/JNEUROSCI.1321-07.2007 (2007).
75. Trautmann, E. M. *et al.* Accurate estimation of neural population dynamics without spike sorting. *Neuron* **103**(2), 292–308. https://doi.org/10.1016/j.neuron.2019.05.003 (2019).
76. Buzsáki, G. & Mizuseki, K. The log-dynamic brain: how skewed distributions affect network operations. *Nat. Rev. Neurosci.* **15**(4), 264–278. https://doi.org/10.1038/nrn3687 (2014).
77. Song, S., Sjöström, P. J., Reigl, M., Nelson, S. & Chklovskii, D. B. Highly nonrandom features of synaptic connectivity in local cortical circuits. *PLOS Biol* **3**, e68. https://doi.org/10.1371/journal.pbio.0030068 (2005).
78. Xia, Y. Chapter Eleven - Correlation and association analyses in microbiome study integrating multiomics in health and disease, In *Progress in Molecular Biology and Translational Science*, vol. 171, J. Sun, Ed., in The Microbiome in Health and Disease, vol. 171., Academic Press, pp. 309–491. doi: (2020). https://doi.org/10.1016/bs.pmbts.2020.04.003
79. Chapin, J. K. & Nicolelis, M. A. L. Principal component analysis of neuronal ensemble activity reveals multidimensional somatosensory representations. *J. Neurosci. Methods* **94**(1), 121–140. https://doi.org/10.1016/S0165-0270(99)00130-2 (1999).

Acknowledgements

This work was supported by a Discovery grant to J.P.T. from the Natural Sciences and Engineering Council of Canada (NSERC Grant No. 210977) and the Gavin Murphy Research Fund (Ottawa Hospital Research Institute, University of Ottawa). Authors are thankful to the laboratory of Dr. Jean-Claude Beïque (University of Ottawa) for infrastructure and technical support.

Author contributions

M.B.R. and J.P.T. conceived the study. M.B.R. and J.S. performed the experiments and data collection. M.B.R. and J.P.T. analyzed the data. V.N. and J.P.T. supervised the study. All authors contributed to interpreting the results. All authors contributed to writing the manuscript.

Competing interests

The authors declare no competing interests.

Additional information

Correspondence and requests for materials should be addressed to J.-P.T.